# Multi-Wavelength Investigations on Galactic Star Forming Regions

A Thesis Submitted to

**Gujarat University**

for the Degree of

**Doctor of Philosophy**

in

Physics

by

**Lokesh Kumar Dewangan**

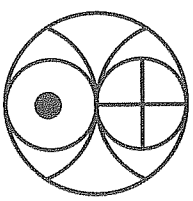

Astronomy and Astrophysics Division

Physical Research Laboratory

Ahmedabad-380 009, India

*Year of Submission : July 2010*

# CERTIFICATE

I hereby declare that the work presented in this thesis is original and carried out by me at Physical Research Laboratory, Ahmedabad. It has not formed the basis for the award of any degree or diploma by any University or Institution.

Dewangan

*Signature of the Candidate*

**Lokesh Kumar Dewangan**

Date: 30-07-2010

Certified by,

*Signature of the Thesis Supervisor*

**Prof. B. G. Anandarao**

Astronomy and Astrophysics Division

Physical Research Laboratory

Navarangpura

Ahmedabad 380009

INDIA

Date: 30. July 2010.

# Contents

**Acknowledgements** i

**List of Figures** viii

**List of Tables** xiii

**1 Introduction** 1

1.1 Star Formation: an overview . . . . . 1

1.1.1 Nucleation sites for star formation . . . . . 2

1.1.2 GMCs and Gravitational Instability . . . . . 3

1.1.3 Low-mass star formation . . . . . 6

1.1.4 High-mass star formation . . . . . 10

1.2 Motivation for the present work . . . . . 16

1.3 Objectives of the Thesis . . . . . 19

1.4 Outline of the thesis . . . . . 20

**2 *Spitzer*-IRAC GLIMPSE study of driving engines of HMPOs and UCHII regions** 22

2.1 The outflow and driving source relationships . . . . . 22

2.1.1 Data Selection and Analysis: The IRCs data sample . . . . . 24

2.1.2 The outflow data . . . . . 26

2.1.3 SED modeling of the IRCs . . . . . 26

2.1.4 Outflow properties vs driving source properties . . . . . 28

2.1.5 Discussion . . . . . 29

2.1.6 Summary and Future Work . . . . . 40

2.2 Physical Properties of the driving engine of Ultra-Compact HII (UCHII) regions . . . . . 41

2.2.1 Data selection . . . . . 41

2.2.2 SED modeling of the driving engines of UCHII regions . . . . . 42
2.2.3 Results and Discussion . . . . . 45
2.2.4 Comparison of SED results: HMPOs and UCHII regions . . . . . 49
2.2.5 Conclusions . . . . . 55

**3 *Spitzer*-IRAC imaging photometric study of the massive star forming region AFGL 437 57**
3.1 Introduction . . . . . 57
3.2 *Spitzer*-IRAC Data on AFGL 437 and Data Reduction . . . . . 59
3.3 Results and Discussion . . . . . 60
3.3.1 Cluster Sources . . . . . 61
3.3.2 IRAC Ratio Maps . . . . . 68
3.3.3 SED modeling of Cluster Sources . . . . . 76
3.4 Conclusions . . . . . 77

**4 A study of the massive star forming region M8 using *Spitzer*-IRAC images 80**
4.1 Introduction . . . . . 80
4.2 *Spitzer*-IRAC Data on Messier 8 and Data Reduction . . . . . 82
4.3 Results and Discussion . . . . . 83
4.3.1 IRAC Photometry . . . . . 83
4.3.2 IRAC Ratio Maps . . . . . 93
4.4 Conclusions . . . . . 98

**5 Infrared photometric study of the massive star forming region S235 100**
5.1 Introduction . . . . . 100
5.2 Observations and Data Analysis . . . . . 102
5.3 Results and Discussion . . . . . 103
5.3.1 IRAC Photometry . . . . . 103
5.3.2 IRAC Ratio Maps . . . . . 126
5.4 Conclusions . . . . . 131

**6 Conclusions and Future Work 133**

**A HMPOs outflow driving engines: Images and SED Modeling 136**

**B Driving engines of UCHII regions: Images and SED Modeling 149**

**C AFGL 437: List of Class II sources; SED modeling of selected sources** **161**

**D M8: IRAC images, YSO lists and YSO selection criteria** **166**

D.1 Criteria for the selection of contaminations: . . . . . 168

D.2 Criteria for the YSO selection: . . . . . 170

D.3 Criteria for the "Red sources": . . . . . 170

**E S235: Supplementary plots, YSO lists and YSO selection criteria** **177**

E.1 Criteria for YSO selection for combined JHK and IRAC data: . . . . . 177

**Bibliography** **190**

**List of Publications** **199**

# List of Figures


1.1 Observational evidences like bipolar outflows and accretion disks associated with low mass stars . . . . . 9
1.2 Classification of low-mass stars based on their Spectral Energy Distributions 10
1.3 The molecular hydrogen ($H_2$) image of IRAS 20126+4104 overlaid with outflow contours . . . . . 17
1.4 The ring structure around the IRS1 of IRAS 20293+3952 using *Spitzer*-IRAC RGB colour-composite image . . . . . 18

2.1 A typical example of the outflow driving engine with its SED . . . . . 30
2.2 a: Observed outflow mass vs total luminosity of the HMPOs. b: Outflow mass vs temperature . . . . . 31
2.3 a: Observed outflow mass vs stellar mass of the HMPOs. b: Outflow momentum vs stellar mass . . . . . 32
2.4 a: Observed outflow mass vs stellar age of the HMPOs. b: Outflow momentum vs stellar age . . . . . 33
2.5 a: Observed outflow mass vs envelope accretion rate of the HMPOs. b: Outflow momentum vs envelope accretion rate . . . . . 34
2.6 a: Observed outflow mass vs disk accretion rate of the HMPOs. b: Outflow momentum vs disk accretion rate. . . . . 35
2.7 a: Observed outflow mass vs envelope mass of the HMPOs. b: Outflow mass vs disk mass. . . . . 36
2.8 a: Observed outflow entrainment rate vs envelope accretion rate of the HMPOs. b: Outflow entrainment rate vs disk accretion rate. . . . . 37
2.9 An example of a driving engine of the UCHII region G10.84-2.59 using IRAC 3-colour-composite image with its SED . . . . . 45
2.10 Histograms of physical parameters: a) stellar mass; b) stellar age and c) stellar temperature for all the 56 sources . . . . . 46

2.11 Exhibits the stellar luminosity vs stellar temperature (H-R diagram) . . . 48
2.12 a: Shows model-derived total luminosity vs mass of the driving engines of the sample UCHII regions. b: The Scatter diagram shows the model-derived stellar temperature vs stellar radius . . . . . 50
2.13 a: The Scatter diagram shows the model-derived stellar mass vs stellar radius for the driving engine of the UCHII regions. b: The Scatter diagram shows the model-derived disk mass vs stellar age . . . . . 51
2.14 a: The Scatter diagram shows the model-derived envelope mass vs stellar age for the driving engine of the UCHII regions. b: The Scatter diagram shows the model-derived disk accretion rate vs stellar age . . . . . 52
2.15 a: The Scatter diagram shows the model-derived envelope accretion rate vs stellar age for the driving engine of the UCHII regions. b: The Scatter diagram shows the model-derived disk accretion rate vs stellar radius . . . 53
2.16 a: The Scatter diagram shows the model-derived envelope accretion rate vs stellar radius for the driving engine of the UCHII regions. b: The Scatter diagram shows the model-derived disk accretion rate vs stellar mass. . . . 54
2.17 The Scatter diagram shows the model-derived envelope accretion rate vs stellar mass for the driving engine of the UCHII regions. . . . . 55

3.1 IRAC images of AFGL 437 are shown in all four channels . . . . . 62
3.2 RGB colour-composite IRAC image of AFGL 437 overlaid with surface density contours . . . . . 63
3.3 The compact cluster is shown in a colour-composite zoomed-in image of AFGL 437 . . . . . 64
3.4 Mid-IR colour-colour diagram constructed using the *Spitzer*-IRAC bands in AFGL 437 . . . . . 66
3.5 Histogram of spectral index ($\alpha_{IRAC}$) of sources in AFGL 437 . . . . . 67
3.6 a: The Empirical cumulative distribution function of nearest-neighbour distance for the all identified YSOs in the whole AFGL 437 region. b: IRAC Ch1 overlaid with surface density contours and positions of YSOs . 69
3.7 IRAC bands encompassing several molecular hydrogen lines . . . . . 73
3.8 IRAC Ch2/Ch4 (a) and Ch4/Ch2 (b) ratio images in the AFGL 437 region 74
3.9 IRAC 8 $\mu$m zoomed-in image of the cluster in AFGL 437 is shown in log scale overlaid by the contours of IRAC ratio image of (Ch2/Ch4) . . . . . 75

3.10 Spectral Energy Distributions for four YSOs in the central cluster: AFGL 437W, S (top panels) N and WK34 (bottom panels) . . . . . 78

4.1 *Spitzer*-IRAC Ch4 (8.0 $\mu$m) image of Lagoon Nebula region . . . . . 84
4.2 Histogram of spectral index ($\alpha_{IRAC}$) of sources in M8 is shown here with regions of different evolutionary stages of star formation shown by vertical lines (see text for more details). Dotted line represents the distribution of photospheric sources and distribution of YSOs is shown by solid line. . . 86
4.3 Mid-IR colour-colour diagram using the *Spitzer*-IRAC bands for all the sources identified within the M8 region . . . . . 88
4.4 a: *Spitzer*-IRAC field of M8 showing all the 327 sources. b: *Spitzer*-IRAC field of M8 showing contaminants . . . . . 89
4.5 a: Empirical cumulative distribution function of nearest-neighbour distance for the YSOs. b: The inflection distance $d_c$ = 0.75 pc is used to distinguish the clustered and scattered members . . . . . 91
4.6 *Spitzer*-IRAC Ch3 (5.8 $\mu$m) image of M8 superposed by IRAC Class 0/I and II sources and sub-mm gas clumps . . . . . 92
4.7 Ratio image of Ch2/Ch4 of M8 (Lagoon Nebula) overlaid by HST H$\alpha$ (F656N filter) contours, in a region around Her 36 . . . . . 95
4.8 Ratio image of Ch4/Ch2 of M8 (Lagoon Nebula) . . . . . 96
4.9 Ratio maps of Ch1/Ch2 in log scale, showing the ridges and filamentary structures (towards east/south-east of Her 36) . . . . . 97
4.10 Ratio maps of Ch3/Ch2 in log scale, showing the ridges and filamentary structures (towards east/south-east of Her 36) . . . . . 98
4.11 Ratio maps of Ch4/Ch2 in log scale, showing the ridges and filamentary structures (towards east/south-east of Her 36) . . . . . 99

5.1 IRAC 3-colour-composite image (size $\sim$ 22.5 $\times$ 16.6 arcmin$^2$) of S235 complex . . . . . 104
5.2 Histogram of spectral index ($\alpha_{IRAC}$) of sources in S235 complex . . . . . 106
5.3 Mid-IR colour-colour diagram using the *Spitzer*-IRAC bands for all the sources identified within the region shown in Fig. 5.1 . . . . . 107
5.4 *Spitzer*-IRAC Ch2 (4.5 $\mu$m) image of S235 (similar size as shown in Fig. 5.1) over-plotted by IRAC Class 0/I and II sources . . . . . 108
5.5 a: *Spitzer*-IRAC S235 region with distribution of all the 286 sources. b: *Spitzer*-IRAC S235 region showing contaminants . . . . . 109

5.6 IRAC 3-colour-composite (Ch4(red), Ch2(green) and Ch1(blue)) zoomed-in image of East 1 region (Fig. 5.1: dashed box) . . . . . 110
5.7 IRAC 3-colour-composite (Ch4(red), Ch2(green) and Ch1(blue)) zoomed-in image of East 2 region (Fig. 5.1: dotted box) . . . . . 112
5.8 SED model plots of selected sources in the East 1 and East 2 regions are shown here . . . . . 113
5.9 IRAC 3-colour-composite (Ch4(red), Ch2(green) and Ch1(blue)) zoomed-in image of S235A-B region (shown in Fig. 5.1 by solid box) . . . . . 116
5.10 Exhibits the Mt. Abu NIR 3-colour-composite K(red), H(green) and J(blue) image of the vicinity of S235A-B region . . . . . 117
5.11 De-reddened colour-colour diagram with identified new YSOs (Class I and Class II) in the S235A-B region . . . . . 118
5.12 Newly identified YSOs (see Figure 5.11) are overlaid on the 3-colour-composite image (K-band (blue), Ch1 (green) and Ch2 (red)) . . . . . 119
5.13 Surface density map of YSOs overlaid on IRAC Ch2 image . . . . . 121
5.14 a: The plot is the same as the one shown in Fig. 5.13., except that the image is removed. b: The distribution of all cluster members with $d_c$ (0.33 pc) . 122
5.15 The image on the left represents the zoomed-in IRAC ratio map of Ch2/Ch4 in a region showed by the dashed box in Fig. 5.12. Right side image shows the positions of sources seen atleast in any one of the IRAC bands with contours (red) of IRAC Ch4 image overlaid having levels between min = 420 and max = 1300 MJy/Sr . . . . . 124
5.16 SED model plots of selected sources in the S235A-B region (labeled in Fig. 5.9) . . . . . 125
5.17 IRAC ratio map of Ch2/Ch4 for the entire S235 complex. Box regions marked here are shown zoomed-in Figs. 5.18, 5.19 and 5.20. . . . . 127
5.18 IRAC ratio map of Ch2/Ch4 in East 1 region revealing bright regions . . . 128
5.19 IRAC ratio map of Ch2/Ch4 in East 2 region revealing bright regions . . . 129
5.20 IRAC ratio map of Ch2/Ch4 in the S235A-B region revealing bright regions 130

A.1 Outflow associations for 13 IRC(s). *Spitzer*-IRAC 8$\mu$m images of the IRC(s) are represented by grey scale . . . . . 137
A.2 Outflow associations for 6 IRC(s) for which *Spitzer*-IRAC data are unavailable. 2MASS K-band images are represented by grey scale . . . . . 138

A.3 3-colour-composite *Spitzer*-IRAC images made from Ch4, Ch2 and Ch1 shown as red, green and blue respectively . . . . . 139
A.4 3-colour-composite *Spitzer*-IRAC images Ch4 (red), Ch2 (green) and Ch1 (blue) for three sources; and 2MASS K(red), H(green) and J(blue) images for one source namely, IRAS 05553+1631. . . . . 140
A.5 SED model plots . . . . . 141
A.6 The best fit SED models are shown decomposed into the disk (green), envelope (red) and scattered light (yellow) components . . . . . 145

B.1 *Spitzer*-IRAC 3-colour-composite images of UCHII regions (Ch4(red), Ch2(green) and Ch1(blue)) . . . . . 150
B.2 SED model plots of the driving engine of UCHII regions (plot details are the same as in Fig A.5) . . . . . 154

C.1 SED model plots of s1-s9 sources (from Table 3.1) and details of the plots are the same as in Fig A.5 . . . . . 163
C.2 SED model plots of s10-s17 (from Table 3.1) and details of the plots are the same as in Fig A.5 . . . . . 164

D.1 *Spitzer*-IRAC 3-colour-composite image of the entire M8 region . . . . . 167

E.1 Empirical cumulative distribution function of nearest-neighbour distance for the YSOs in the entire S235 complex . . . . . 179
E.2 Colour-colour diagram used for measuring extinction for dereddening . . 180
E.3 Empirical cumulative distribution function of nearest-neighbour distance for the YSOs in Mt. Abu NIR observed region (the vicinity of S235A-B) . 181

# List of Tables


1.1 Phases of ISM . . . . . 3
1.2 Physical properties of clouds, clumps and cores . . . . . 4
1.3 Jeans mass, size and free-fall time for clumps and cores . . . . . 6

2.1 List of 33 driving engines of the molecular outflows and their positions . . 25
2.2 Driving engines of the UCHII regions with their positions and offsets(in arcsec) from the sub-mm peaks . . . . . 43

3.1 *Spitzer*-IRAC photometry (in mag) of the YSOs identified in the central cluster of AFGL 437 . . . . . 70
3.2 Important $H_2$ and PAH lines in IRAC bands . . . . . 72
3.3 Physical parameters derived from SED modeling of the main sources AFGL 437 W,S,N and WK34 (see text) . . . . . 77

5.1 Some of the selected sources in S235 East 1 region . . . . . 114
5.2 Physical parameters derived from SED modeling of the labeled sources from Table 5.1 in S235 East 1 region . . . . . 114
5.3 Some of the selected sources in S235 East 2 region . . . . . 114
5.4 Physical parameters derived from SED modeling of the labeled sources from Table 5.3 in S235 East 2 region . . . . . 114
5.5 Some of the selected sources in S235A-B region . . . . . 125
5.6 Physical parameters derived from SED modeling of the labeled sources from Table 5.5 in S235A-B region . . . . . 126

A.1 Physical parameters of the HMPO sources . . . . . 148

B.1 Physical parameters of the driving engine(s) of UCHII regions . . . . . 159

C.1 *Spitzer*-IRAC 4-channel photometry (in mag) of the Class II sources in the AFGL 437 region . . . . . 162

C.2 Physical parameters derived from SED modeling of the 17 sources (s1-s17) 165

D.1 *Spitzer*-IRAC 4-channel photometry (in mag) of the Class 0/I YSOs identified in the M8 . . . . . 171

D.2 *Spitzer*-IRAC 4-channel photometry (in mag) of the Class II YSOs identified in the M8 . . . . . 173

E.1 *Spitzer*-IRAC photometry (in mag) of the Class 0/I YSOs identified in S235 182

E.2 *Spitzer*-IRAC photometry (in mag) of the Class II YSOs identified in S235 complex . . . . . 184

E.3 Mt. Abu J, H, K and *Spitzer*-IRAC Ch1 and Ch2 band photometry (in mag) of the Class I YSOs identified in vicinity of S235A-B region . . . . . 188

E.4 Mt. Abu J, H, K and *Spitzer*-IRAC Ch1 and Ch2 band photometry (in mag) of the Class II YSOs identified in vicinity of S235A-B region . . . . . 189